



**HAL**  
open science

# Neural-Network-based Kalman Filters for the Spatio-Temporal Interpolation of Satellite-derived Sea Surface Temperature

Said Ouala, Ronan Fablet, Cédric Herzet, Bertrand Chapron, Ananda Pascual, Fabrice Collard, Lucile Gaultier

► **To cite this version:**

Said Ouala, Ronan Fablet, Cédric Herzet, Bertrand Chapron, Ananda Pascual, et al.. Neural-Network-based Kalman Filters for the Spatio-Temporal Interpolation of Satellite-derived Sea Surface Temperature. *Remote Sensing*, 2018, 10 (12), pp.1864. 10.3390/rs10121864 . hal-01896654

**HAL Id: hal-01896654**

<https://imt-atlantique.hal.science/hal-01896654v1>


Submitted on 16 Oct 2018

**HAL** is a multi-disciplinary open access archive for the deposit and dissemination of scientific research documents, whether they are published or not. The documents may come from teaching and research institutions in France or abroad, or from public or private research centers.

L'archive ouverte pluridisciplinaire **HAL**, est destinée au dépôt et à la diffusion de documents scientifiques de niveau recherche, publiés ou non, émanant des établissements d'enseignement et de recherche français ou étrangers, des laboratoires publics ou privés.

Article

# Neural-Network-based Kalman Filters for the Spatio-Temporal Interpolation of Satellite-derived Sea Surface Temperature

Said Ouala <sup>1\*</sup> , Ronan Fablet <sup>2</sup>, Cédric Herzet <sup>3</sup>, Bertrand Chapron <sup>4</sup>, Ananda Pascual <sup>5</sup>, Fabrice Collard <sup>6</sup>, Lucile Gaultier <sup>7</sup>

<sup>1</sup> IMT Atlantique, Lab-STICC, UBL, Brest, France; said.ouala@imt-atlantique.fr

<sup>2</sup> IMT Atlantique, Lab-STICC, UBL, Brest, France; ronan.fablet@imt-atlantique.fr

<sup>3</sup> IMT Atlantique, Lab-STICC, UBL, Brest; INRIA Bretagne-Atlantique, SIMSMART, Rennes, France; cedric.herzet@inria.fr

<sup>4</sup> Ifremer, LOPS, Brest, France; Bertrand.Chapron@ifremer.fr

<sup>5</sup> IMEDEA, UIB-CSIC, Esporles, Spain; ananda.pascual@imedea.uib-csic.es

<sup>6</sup> ODL, Brest, France; dr.fab@oceandatalab.com

<sup>7</sup> ODL, Brest, France; lucile.gaultier@oceandatalab.com

\* Correspondence: said.ouala@imt-atlantique.fr

Version October 15, 2018 submitted to Remote Sens.

**Abstract:** In this work we address the reconstruction of gap-free Sea Surface Temperature (SST) fields from irregularly-sampled satellite-derived observations. We develop novel Neural-Network-based (NN-based) Kalman filters for spatio-temporal interpolation issues as an alternative to ensemble Kalman filters (EnKF). The key features of the proposed approach are two-fold: the learning of a probabilistic NN-based representation of 2D geophysical dynamics, the associated parametric Kalman-like filtering scheme for a computationally-efficient spatio-temporal interpolation of Sea Surface Temperature (SST) fields. We illustrate the relevance of our contribution for an OSSE (Observing System Simulation Experiment) in a case-study region off South Africa. Our numerical experiments report significant improvements in terms of reconstruction performance compared with operational and state-of-the-art schemes (e.g., optimal interpolation, Empirical Orthogonal Function (EOF) based interpolation and analog data assimilation).

**Keywords:** Data assimilation; Dynamical model; Kalman filter; Neural networks; Data-driven models; Interpolation

## 1. Introduction

Satellite sensors and in-situ networks can provide observations of sea surface tracers (e.g. temperature, salinity, ocean colour). However, due to sensors's characteristics (e.g., space-time sampling, sensor type) and their sensitivity to the atmospheric conditions (e.g., rain, clouds), only partial and possibly noisy observations are available. As a consequence, no sensor can provide gap-free high-resolution observations in space and time. A typical example of the missing data pattern for SST is reported in Fig. 3 for an infrared sensor. In some situations, missing data may become very large which makes crucial the development of spatio-temporal interpolation tools.

Within the satellite ocean community, Optimal interpolation (OI) is the standard technique [1–7]. Given a covariance model of spatio-temporal dynamics, the interpolated field results from a linear combination of the observations. The parameters of the linear combination are typically tuned by exploiting some statistical properties of the target field.

26 In general, stationary covariance hypotheses are considered, which prove relevant for the  
27 reconstruction of horizontal scales above 100km. Fine scale components may hardly be retrieved  
28 with such approaches and a variety of research studies aim to improve the reconstruction of the  
29 high-resolution component of our spatio-temporal fields.

30 Empirical Orthogonal Function (EOF) based interpolation is an other categorie widely used in  
31 geosciences [8–10]. They rely on a Singular Value Decomposition (SVD) to compute the EOF basis, the  
32 field is then reconstructed by projecting the observations on the EOF subspace until a convergence  
33 criterion is reached [11]. Unfortunately, dealing with high missing data rates decreases the encoded  
34 variability in the EOF components witch results in smoothing fine scale components.

35 Data assimilation is the state-of-the-art framework for the reconstruction of dynamical systems  
36 from partial observations based on a given numerical model [12,13]. Statistical data assimilation  
37 schemes especially ensemble Kalman filters, have become particularly popular due to their trade-off  
38 between computational efficiency and modeling flexibility. Unlike OI and EOF based techniques,  
39 these schemes explicitly rely on dynamical priors to address interpolation issues from partial and  
40 noisy observations. When dealing with sea surface dynamics, the analytical derivation of these  
41 priors involves simplifying assumptions which may not be satisfied by real observations. By contrast,  
42 realistic analytical parameterizations may lead to highly computationally-demanding numerical  
43 models associated with modeling and inversion uncertainties, which may limit their relevance for an  
44 application of the interpolation of a single sea surface tracer.

45 Recently, data-driven approaches [8,14] have emerged as relevant alternatives to model-driven  
46 schemes. They take benefit from the increasing availability of remote sensing observation and  
47 simulation data to derive dynamical priors from these datasets. Analog methods are one of the first  
48 data-driven techniques to develop this data-driven paradigm within a data assimilation framework  
49 [14]. Analog forecasting operators provide a data-driven formulation of the dynamical operator, which  
50 can be used as a plug-and-play operator in Kalman-based assimilation schemes. Combined with  
51 patch-based representation, the analog data assimilation was recently proven to be relevant with  
52 respect to OI and EOF-based schemes for the spatio-temporal interpolation of sea surface geophysical  
53 tracers [15–17].

54 In this paper, we further investigate data-driven interpolation approaches within a statistical  
55 data assimilation framework. We focus on neural network and deep learning models, which have  
56 rapidly become the state-of-the-art in machine learning for a wide range of applications, including  
57 inverse imaging issues [18]. Recent applications to the assimilation of low-dimensional dynamical  
58 systems [19] and to the forecasting of geophysical dynamics [20] have been developed. However,  
59 to our knowledge, the design of neural-network-based assimilation models for the spatio-temporal  
60 interpolation of geophysical dynamics remain an open challenge, which may greatly benefit from the  
61 ability of deep learning models to capture computationally-efficient representations from available  
62 ocean observation and simulation datasets. In this study, we address this challenge and propose a novel  
63 NN-based Kalman filtering scheme applied to the spatio-temporal interpolation of satellite-derived  
64 sea surface temperature. We exploit a ResNet architecture [19,21] and a patch-based decomposition  
65 [22] to derive a data-driven representation of spatio-temporal fields. Importantly, this architecture  
66 conveys a probabilistic representation through the prediction of a mean component and a covariance  
67 pattern. The later may be regarded as a NN-based representation of the covariance patterns issued  
68 from Monte Carlo approximations in ensemble assimilation schemes [23]. Overall, the methodological  
69 contributions of this work are two-fold: i) we propose a new probabilistic NN-based representation  
70 of 2D geophysical dynamics, ii) we derive the associated NN-based Kalman filtering scheme for  
71 spatio-temporal interpolation issues. We demonstrate the relevance of these contributions with respect  
72 to state-of-the-art approaches [2,8,16] for the spatio-temporal interpolation of satellite-derived SST  
73 fields in a case study region off South Africa. This paper is organized as follows. Section 2 reviews  
74 data assimilation schemes. Section 3 describes the proposed neural-network-based data assimilation

75 framework. Section 4 presents the results of the numerical experiments. We further discuss our  
76 contributions in Section 6.

## 77 2. Problem statement and related work

78 Regarding ocean remote sensing data, spatio-temporal interpolation issues can be regarded as the  
79 reconstruction of some hidden states from partial and/or noisy observation series, referred to as data  
80 assimilation in geoscience [23]. Data assimilation techniques usually involve a state-space evolution  
81 model [23]:

$$x_{t+1} = \mathcal{F}(x_t) + \eta_t \quad (1)$$

$$y_{t+1} = \mathcal{H}(x_{t+1}) + \epsilon_t \quad (2)$$

82 where  $t \in \{0, \dots, T\}$  represents the temporal resolution of our time series and  $\mathcal{F}$  the dynamical  
83 model describing the temporal evolution of the physical variables  $x$ . The observation model  $\mathcal{H}$  links the  
84 observation  $y$  to the physical variable  $x$ .  $\eta_t$  and  $\epsilon_t$  are random processes accounting for the uncertainties  
85 in the dynamical and observation models. They are usually defined as centered Gaussian processes  
86 with covariances  $Q_t$  and  $R_t$  respectively.

87 From a probabilistic point of view, the spatio-temporal interpolation problem can be seen  
88 as a Bayesian filtering problem where the main goal is to evaluate the conditional probabilities  
89  $p(x_{t+1}|y_1, \dots, y_t)$  (prediction distribution of the state  $x_{t+1}$  given observations up to time  $t$ ) and  
90  $p(x_{t+1}|y_1, \dots, y_t, y_{t+1})$  (posterior distribution of  $x_{t+1}$  given observations up to time  $t + 1$ ). Under  
91 certain assumptions over the state space model (the dynamical and observation models are linear  
92 with Gaussian uncertainties), the prediction and posterior distributions are also Gaussian and can be  
93 written as :

$$p(x_{t+1}|y_1, \dots, y_t) = \mathcal{N}(x_{t+1}^-, \Sigma_{t+1}^-) \quad (3)$$

$$p(x_{t+1}|y_1, \dots, y_{t+1}) = \mathcal{N}(x_{t+1}^+, \Sigma_{t+1}^+) \quad (4)$$

94 with the means and covariances computed for each time  $t$  using the well known Kalman recursion

$$x_{t+1}^- = Fx_t^+ \quad (5)$$

$$\Sigma_{t+1}^- = F\Sigma_t^+ F^T + Q_t \quad (6)$$

$$x_{t+1}^+ = x_{t+1}^- + K_{t+1}[y_{t+1} - H_{t+1}x_{t+1}^-] \quad (7)$$

$$\Sigma_{t+1}^+ = \Sigma_{t+1}^- - K_{t+1}H_{t+1}\Sigma_{t+1}^- \quad (8)$$

95 with

$$K_{t+1} = \Sigma_{t+1}^- H_{t+1}^T [H_{t+1} \Sigma_{t+1}^- H_{t+1}^T + R_t]^{-1}. \quad (9)$$

96 Here  $F$  and  $H_{t+1}$  corresponds respectively to some linear dynamical and observation models. The  
97 superscript (-) refers to the forecasting of the mean of the state variable  $x_{t+1}^-$  and of its covariance matrix  
98  $\Sigma_{t+1}^-$  given observations up to time  $t$  but without the new observation at time  $t + 1$ . The superscript (+)  
99 refers in the other hand to the mean of the state variable  $x_{t+1}^+$  and of the covariance matrix  $\Sigma_{t+1}^+$  given  
100 all observations up to time  $t + 1$ . They are referred to as the assimilated mean and covariance.  $K_{t+1}$  is  
101 the Kalman gain. Kalman filters provide a sequential formulation of the Optimal Interpolation (OI)  
102 [24] which may also be solved directly knowing the space-time covariance of processes  $x$  and  $y$ . For

103 non-linear and high-dimensional dynamical systems, the pdfs are not Gaussian anymore and the above  
 104 Kalman recursion does define their means and covariances. Ensemble Kalman methods have been  
 105 proposed to address these issues. The ensemble Kalman filter and smoother [23] are the first sequential  
 106 filtering techniques used reliably in the reconstruction of geophysical fields. The key idea here is to  
 107 approximate the forecasting mean  $x_{t+1}^-$  and covariance  $\Sigma_{t+1}^-$  by a sample mean and covariance matrix  
 108 computed by propagating an ensemble of  $M$  members,  $\{x_{t+1}^{i-}\}_{i=1}^M$ , using the dynamical model  $\mathcal{F}$ .

$$x_{t+1}^{i-} = \mathcal{F}(x_t^{i+}, i \in \{0, \dots, N\}) \quad (10)$$

$$\Sigma_{t+1}^- = \frac{1}{N-1} D_{t+1} D_{t+1}^T \quad (11)$$

$$D_{t+1} = [x_{t+1}^{1-} - x_{t+1}^-, \dots, x_{t+1}^{N-} - x_{t+1}^-] \quad (12)$$

$$x_{t+1}^{i+} = x_{t+1}^{i-} + K_{t+1} [y_{t+1} - H_{t+1} x_{t+1}^{i-}] \quad (13)$$

$$K_{t+1} = \Sigma_{t+1}^- H_{t+1}^T [H_{t+1} \Sigma_{t+1}^- H_{t+1}^T + R_t]^{-1} \quad (14)$$

$$\Sigma_{t+1}^+ = \Sigma_{t+1}^- - K_{t+1} H_{t+1} \Sigma_{t+1}^- \quad (15)$$

109 Besides all its advantages, EnKF techniques do not escape the curse of dimensionality.  
 110 High-dimensional systems require using large ensemble sizes  $M$  which may lead to very  
 111 high-computational complexity. The use of small ensemble sizes in the other hand may result in  
 112 undersampling the covariance matrix (the considered ensemble is not representative of our systems  
 113 dynamics) which may in turn result in poor reconstruction performance, including for instance  
 114 filter divergence and spurious long-range correlations. Proposed solutions such as inflation [25],  
 115 cross-validation [26] and localization methods [27–29] may require thorough tuning experiments.  
 116 An alternative strategy based on a model-driven propagation of parametric covariance models  
 117 [30,31] seems appealing. Using advection priors [32], it propagates parametric covariance structures,  
 118 which leads to the implementation of the classic Kalman recursion. Accounting for more complex  
 119 dynamical priors for the covariance structure is an open question, which may limit the applicability  
 120 of this approach to complex geophysical systems. Inspired by the later parametric framework,  
 121 we aim to design an efficient sequential filtering technique for the reconstruction of geophysical  
 122 fields. Rather than considering a model-driven prior to propagate Gaussian states as in [30,31], we  
 123 investigate NN-based priors, which may be fitted from training data. The resulting NN-based Gaussian  
 124 representations provide computationally-efficient approximations of the dynamical priors that should  
 125 prevent undersampling issues within a Kalman recursion.

### 126 3. Proposed interpolation model

#### 127 3.1. Neural-network Gaussian dynamical prior

128 Our key idea is to exploit neural-network (NN) representations for the time propagation of  
 129 a Gaussian approximation of the distribution of the state. Compared with dynamical priors in  
 130 assimilation model (1), which state conditional distribution  $x_t | x_{t-1}$ , we here consider neural-network  
 131 representations to extend the prediction step of the Kalman recursion (5-6) to non-linear dynamics.  
 132 Formally, it comes to define:

$$x_{t+1}^- = \mathcal{F}(x_t^+) \quad (16)$$

$$\Sigma_{t+1}^- = \mathcal{F}_\Sigma(x_t^+, \Sigma_t^+) \quad (17)$$

133 with  $x_{t+1}^-$  and  $\Sigma_{t+1}^-$  the mean and covariance of the prediction of the Gaussian approximation  
 134 of the state at time  $t + 1$  given the assimilated mean  $x_t^+$  and covariance  $\Sigma_t^+$  at time  $t$ . Functions  
 135  $\mathcal{F}, \mathcal{F}_\Sigma$  are neural networks to be defined with parameter vectors  $\theta = (\theta_\mu, \theta_\Sigma)$ . It may noted that our

136 parameterization follows (5-6) such that the update of the mean component in (16) only depends on  
 137 the mean at the previous time step and the update of the covariance depends both on the mean and  
 138 covariance at the previous time step. Given this NN-based representation of the prediction step of the  
 139 Kalman filter, we apply the classic Kalman-based filtering under the assumption that the observation  
 140 model is linear and Gaussian:

$$x_{t+1}^+ = x_{t+1}^- + K_{t+1}[y_{t+1} - H_{t+1}x_{t+1}^-] \quad (18)$$

$$K_{t+1} = \Sigma_{t+1}^- H_{t+1}^T [H_{t+1} \Sigma_{t+1}^- H_{t+1}^T + R_t]^{-1} \quad (19)$$

141 Such a formulation does not require forecasting an ensemble to compute a sample covariance  
 142 matrix. It results in a significant reduction of the computational complexity. The same holds when  
 143 compared to the computational complexity of the analog data assimilation which involves ensemble  
 144 forecasting and repeated nearest-neighbor search.

### 145 3.2. Patch-based NN architecture

146 When considering spatio-temporal fields, the application of the model defined by (16) and  
 147 (17) should be considered with care to account for the underlying dimensionality, especially for the  
 148 covariance model in (19). Following our previous works on analog data assimilation [15,16], we  
 149 consider a patch-based representation<sup>1</sup>. This patch-based representation is fully embedded in the  
 150 considered NN architecture to make explicit both the extraction of the patches from a 2D field and the  
 151 reconstruction of a 2D field from the collection of patches. The later involves a reconstruction operator  
 152 which is learnt from data.

153 Regarding model  $\mathcal{F}$ , the proposed architecture proceeds as follows:

- 154 • At a given time  $t$ , the first layer of the network, which is parameter-free in terms of training,  
 155 comes to decompose an input field  $x_t$  into a collection of  $N_p$   $P \times P$  patches  $x_{\mathcal{P}_s,t}$ , where  $P$  is  
 156 the width and height of each patch and  $s$  the patch location in the global field. Each patch is  
 157 decomposed onto an EOF basis  $\mathcal{B}$  according to :

$$z_{\mathcal{P}_s,t} = x_{\mathcal{P}_s,t} \mathcal{B}^T \quad (20)$$

158 with  $z_{\mathcal{P}_s,t}$  the EOF decomposition of the patch  $x_{\mathcal{P}_s,t}$ . The EOF decomposition matrix  $\mathcal{B}$  is trained  
 159 offline as preprocessing step;

- 160 • The second layer implements a numerical integration scheme (typically, an Euler or 4th-order  
 161 Runge-Kutta scheme) using a patch-level dynamical model  $\mathcal{F}^{\mathcal{P}_s}$ ,  $s \in [1, \dots, N_p]$  to predict  
 162  $z_{\mathcal{P}_s,t+1}$ . For patch-level models  $\mathcal{F}^{\mathcal{P}_s}$ , we consider residual architectures [21] with a bilinear  
 163 parameterization [19];
- 164 • The third layer is a reconstruction network  $\mathcal{F}_r$ . It combines the predicted patches  $x_{\mathcal{P}_s,t} =$   
 165  $z_{\mathcal{P}_s,t} \mathcal{B}$ ,  $s \in [1, \dots, N_p]$  to reconstruct the output field  $x_t$ . This reconstruction network  $\mathcal{F}_r$  involves a  
 166 convolution neural network [33].

167 The details of the considered parameterizations for the second and third layers are given in  
 168 Section 4. To train mean dynamical model  $\mathcal{F}$ , we apply a two-step procedure. We first learn the local  
 169 dynamical models  $\mathcal{F}^{\mathcal{P}_s}$ ,  $s \in [1, \dots, N_p]$  based on the minimization of the EOF-patch based forecasting  
 170 error. The reconstruction network  $\mathcal{F}_r$  is then optimized using the same criterion over the global field.

---

<sup>1</sup> A patch is a  $P \times P$  subregion of a 2D field with  $P$  the width and the height of the patch.

171 Regarding covariance model  $\mathcal{F}_\Sigma$  we also consider a patch-based representation of the spatial  
 172 domain  $\mathcal{F}_\Sigma^{\mathcal{P}_s}$ , more precisely a block-diagonal parameterization of the patch-level covariances in the  
 173 EOF space. It may be noted that a diagonal parameterization of the covariance in the EOF space forms  
 174 a full covariance matrix in the original patch space. This block-diagonal covariance model  $\mathcal{F}_\Sigma$  is learnt  
 175 separately for each patch according to a ML (Maximum Likelihood) criterion. The associated training  
 176 dataset comprises patch-based EOF decompositions of the forecasted states according to the mean  
 177 model  $\mathcal{F}^{\mathcal{P}_s}$  from states of the training dataset corrupted by an additive Gaussian perturbation with a  
 178 covariance structure  $\Sigma_0$ . Here,  $\Sigma_0$  is given by the empirical covariance of the EOF patches for the entire  
 179 training dataset. Overall, for a given patch  $\mathcal{P}_s$ , we parameterize  $\mathcal{F}_\Sigma^{\mathcal{P}_s}$  the restriction of covariance  $\mathcal{F}_\Sigma$   
 180 onto patch  $\mathcal{P}_s$  as:

$$\mathcal{F}_\Sigma^{\mathcal{P}_s}(x_{\mathcal{P}_s,t+1}, \Sigma_{\mathcal{P}_s,t+1}) = \mathcal{B}^t \Psi(\Sigma_{\mathcal{P}_s,t}, \Sigma_0) \cdot \mathcal{F}_D^{\mathcal{P}_s}(z_{\mathcal{P}_s,t}, \Sigma_0) \cdot \mathcal{B} \quad (21)$$

181 with  $\Psi(\Sigma_{\mathcal{P}_s,t-1}, \Sigma_0)$  a scaling function. Among different parameterizations, a constant scaling  
 182 function  $\Psi() = 1$  led to the best performance in our numerical experiments.

183 To illustrate the relevance of the proposed full covariance matrix parametrization (based on a  
 184 patch based projection on the EOF space and illustrated for instance by equation 21), we also investigate  
 185 a diagonal covariance matrix model in the patch space.

### 186 3.3. Data assimilation procedure

187 Given a trained patch-based NN representation as described in the previous section, we derive  
 188 the associated Kalman-like filtering procedure. As summarized in Algorithm 1, at time step  $t$ , given the  
 189 Gaussian approximation of the posterior likelihood  $P(x_{t-1}|y_0, \dots, y_{t-1})$  with mean  $x_{t-1}^+$  and covariance  
 190  $\Sigma_{t-1}^+$ , we first compute the forecasted Gaussian approximation at time  $t$  with mean field  $\mathcal{F}(x_{t-1}^+)$  and  
 191 patch-based covariance  $\mathcal{F}_\Sigma(x_{t-1}^+, \Sigma_{t-1}^+)$ . The assimilation of the new observation  $y_t$  is performed at  
 192 a patch-level. For each patch  $\mathcal{P}_s$ , we update the patch-level mean  $x_{\mathcal{P}_s,t}^+$  and covariance  $\Sigma_{\mathcal{P}_s,t}^+$  using  
 193 Kalman recursion (8) with observation  $y_{\mathcal{P}_s,t}$ . We then combine these patch-level updates to obtain  
 194 global mean  $x_t^+$  and covariance  $\Sigma_t^+$ . Whereas we compute global mean  $x_t^+$  using trained reconstruction  
 195 network  $\mathcal{F}_r$ ,  $\Sigma_t^+$  just comes to store the collection of patch-level covariances. This procedure is iterated  
 196 up to the end of the observation sequence.

197 Compared with the patch-based analog data assimilation [16], it might be noted that we iterate  
 198 patch-level assimilation steps and global reconstruction steps thanks to the NN-based propagation of  
 199 the patch-based covariance structure. This procedure potentially allows information propagation from  
 200 one patch to neighboring ones after each assimilation step. By contrast, in the patch-based analog  
 201 data assimilation, each patch is processed independently, such that no such information propagation  
 202 can occur. This is regarded as a key feature to account for the propagation of geophysical structures  
 203 (e.g., fronts, eddies, filaments,...).

204 We refer to the patch-based NNKF reconstruction model using the EOF block-diagonal  
 205 parameterization of the covariance model  $\mathcal{F}_\Sigma$ , as model PB-NNKF-EOF. The model using the diagonal  
 206 parameterization of the covariance model  $\mathcal{F}_\Sigma$  in the patch space is referred to as PB-NNKF.

## 207 4. Data and experimental setting

208 As a case-study, we address the spatio-temporal interpolation of satellite-derived SST fields  
 209 associated with infrared sensors, which may involve high missing data rates (typically from 50% to  
 210 90%). We consider the same region and dataset as in [16] to make easier benchmarking analyses.

### 211 4.1. Dataset description

212 As SST time series used here is delivered by the UK Met Office [2] from January 2008 to December  
 213 2015. The spatial resolution of our SST field is  $0.05^\circ$  and the temporal resolution  $h = 1$  day. The data  
 214 from 2008 to 2014 were used as training data and we tested our approach on the 2015 data. To perform

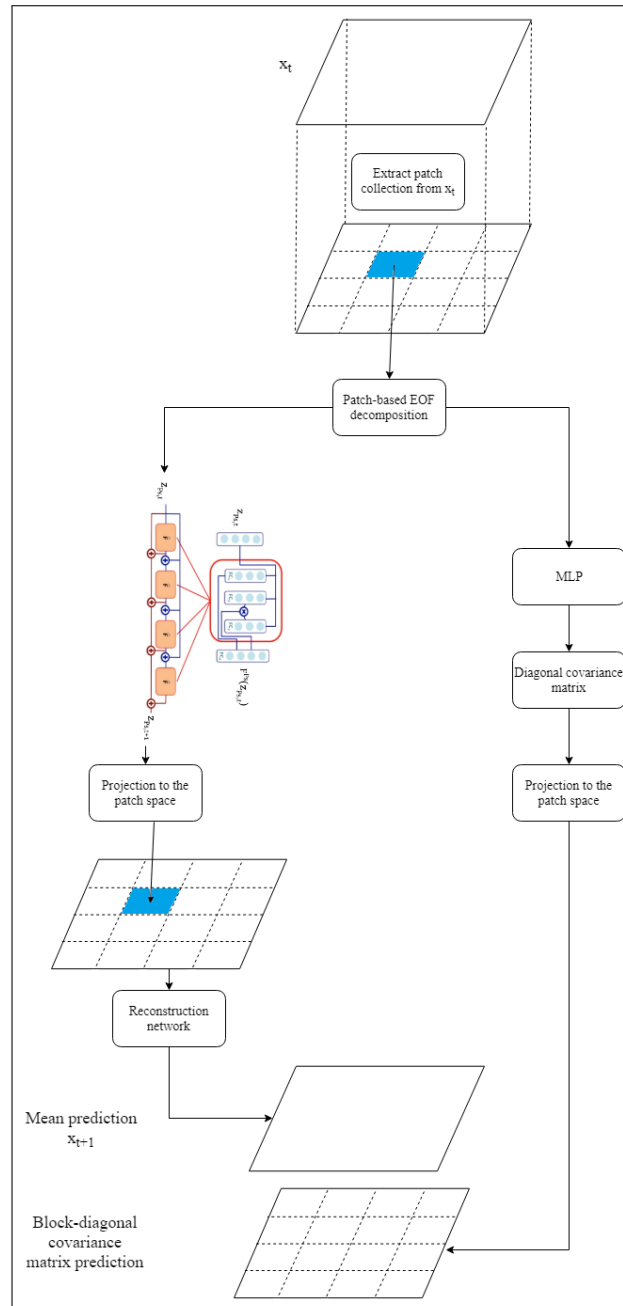


**Figure 1.** Proposed neural-network-based representation of a spatio-temporal dynamical system. The input  $X_t$  is first decomposed into  $P \times P$  patches, each patch is then propagated using its associate local dynamical model. The output  $X_{t+1}$  is then reconstructed by injecting the forecasted patches into the reconstruction model  $\mathcal{F}_r$ .



**Algorithm 1** Patch-based NNKF reconstruction

---

```

1: procedure PB-NNKF( $\mathcal{F}, \mathcal{F}_\Sigma, y, R$ )
2: for  $t$  in  $[0, \dots, T]$ :
3:    $x_t^- \leftarrow \mathcal{F}(x_{t-1}^+)$ 
4:    $[\Sigma_{\mathcal{P}_0, t}^-, \dots, \Sigma_{\mathcal{P}_{N_p}, t}^-] \leftarrow \mathcal{F}_\Sigma(x_{t-1}^+, \Sigma_{t-1}^+)$ 
5:    $[x_{\mathcal{P}_0, t}^-, \dots, x_{\mathcal{P}_{N_p}, t}^-] \leftarrow \text{ExtractPatches}(x_t^-)$ 
6:    $[y_{\mathcal{P}_0, t}, \dots, y_{\mathcal{P}_{N_p}, t}] \leftarrow \text{ExtractPatches}(y_t)$ 
7:   for  $s$  in  $[1, \dots, N_p]$ :
8:      $K_{\mathcal{P}_s, t} = \Sigma_{\mathcal{P}_s, t}^- H_{\mathcal{P}_s, t}^t [H_{\mathcal{P}_s, t} \Sigma_{\mathcal{P}_s, t}^- H_{\mathcal{P}_s, t}^t + R_t]^{-1}$ 
9:      $X_{\mathcal{P}_s, t}^+ = x_{\mathcal{P}_s, t}^- + K_{\mathcal{P}_s, t} [y_{\mathcal{P}_s, t} - H_{\mathcal{P}_s, t} x_{\mathcal{P}_s, t}^-]$ 
10:     $\Sigma_{\mathcal{P}_s, t}^+ = \Sigma_{\mathcal{P}_s, t}^- - K_{\mathcal{P}_s, t} H_{\mathcal{P}_s, t} \Sigma_{\mathcal{P}_s, t}^-$ 
11:     $x_t^+ \leftarrow \text{Reconstruct}([x_{\mathcal{P}_0, t}^+, \dots, x_{\mathcal{P}_{N_s}, t}^+])$ 
12:     $\Sigma_t^+ \leftarrow \text{Reconstruct}([\Sigma_{\mathcal{P}_0, t}^+, \dots, \Sigma_{\mathcal{P}_{N_s}, t}^+])$ 

```

---

215 a quantitative evaluation, we simulated realistic spatio-temporal cloud patterns using METOP-AVHRR  
216 masks. This sensor is highly sensitive to the cloud cover and results in very high missing data rates  
217 as illustrated in Fig. 3. As case-study area, we select an area off South Africa (from  $2.5^\circ E, 38.75^\circ S$   
218 to  $32.5^\circ E, 58.75^\circ S$ ). This region involves complex fine-scale SST dynamics (e.g., fronts, filaments). It  
219 makes it relevant for the considered quantitative evaluation.

220 *4.2. Experimental setting*

221 The proposed neural-network-based Kalman scheme involves the following parameter setting.  
222 The proposed patch-based and NN-based Kalman filter is applied to SST anomaly fields w.r.t.  
223 optimally-interpolated SST fields (see below for the parameterization of the optimal interpolation).  
224 These optimally-interpolated fields provide a relevant reconstruction of horizontal scales up to  $\approx 100$ km.  
225 We exploit patch-level representations with non-overlapping  $20 \times 20$  patches. For each patch  $\mathcal{P}_s$ , we  
226 learn an EOF basis from the training data. We keep the first 50 EOF components, which amount on  
227 average to 95% of the total variance. For the patch-level NN model  $\mathcal{F}^{\mathcal{P}_s}$ , we use a bilinear residual  
228 neural network architecture as proposed in [34] with 60 linear neurons, 100 bilinear neurons and 10  
229 fully-connected layers with a Relu activation. The reconstruction model  $\mathcal{F}_r$  is a convolutional neural  
230 network with 3 convolutional layers. The first two layers comprise 64 filters of size  $3 \times 3$  with a Relu  
231 activation and the last layer is a linear convolutional layer with one filter. Regarding covariance model  
232  $\mathcal{F}_D^{\mathcal{P}_s}$ , we consider a diagonal covariance model within each patch. Each element of diagonal involves  
233 a 3-layer MLP with 4 neurons and Relu activation functions on the hidden layers and a *softplus*  
234 activation in the output layer. With a view to evaluating the EOF-based covariance parameterization,  
235 we consider both PB-NNKF-EOF and PB-NNKF schemes.

236 We perform a quantitative analysis of the interpolation performance of the proposed scheme with  
237 respect to an optimal interpolation, the analog data assimilation [16] and the EOF based interpolation  
238 method VE-DINEOF. The considered parameter setting is as follows:

- 239 • Optimal interpolation (OI) : We use a Gaussian kernel with a spatial correlation length of 100km  
240 and a temporal resolution length of 3 days. These parameters were empirically tuned for the  
241 considered dataset using a cross-validation experiment.
- 242 • Analog data assimilation (LAF-EnKF, GAF-ENKF): We apply both the global and local analog  
243 data assimilation schemes, referred to as G-AnDA and L-AnDA [14,16]. Similarly to the  
244 proposed scheme, we consider  $20 \times 20$  patches and 50-dimensional EOF decomposition with  
245 an overlapping of 10 pixels. We let the reader refer to [14,16] for a detailed description of this  
246 data-driven approach, which relies on nearest-neighbor regression techniques.

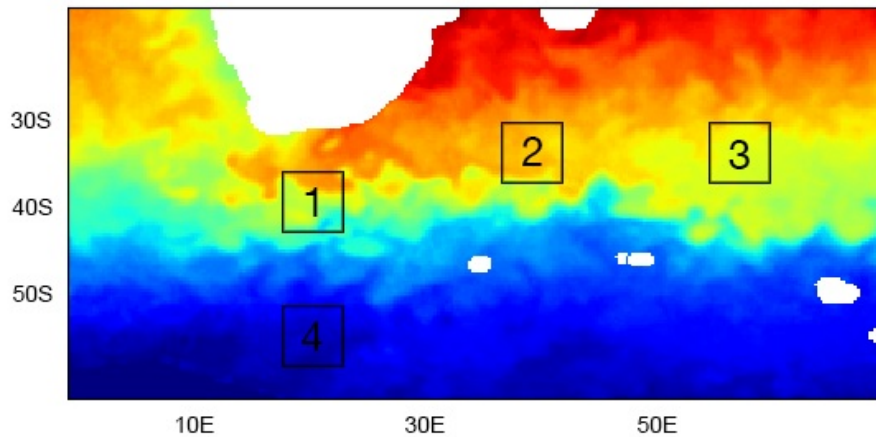


*Figure 2. Selected patches on the high resolution component of the SST data. (The SST map corresponds to July 19, 2015)*

- 247 • EOF based reconstruction (PB-VE-DINEOF): We also compare our approach to the state-of-the-art  
 248 interpolation scheme based on the projection of our observations with missing data on an  
 249 EOF basis [8]. The SST field is here decomposed as described in the analog data assimilation  
 250 application into a collection of  $20 \times 20$  patches with a 10 pixels overlapping. Each patch is then  
 251 reconstructed using the VE-DINEOF method.

## 252 5. Results and discussion

253 We report in this section the results of the considered numerical experiments. We first focus on  
 254 patch-level performance as the patch-based representation is at the core of the proposed interpolation  
 255 model. We then report interpolation performance for the whole case-study region.

### 256 5.1. Patch-level interpolation performance

257 We first evaluate the patch-level interpolation performance of the proposed scheme for four  
 258 patches corresponding to different dynamical modes as illustrated in Fig. 2 located in the area ( $5^{\circ}E$   
 259 to  $75^{\circ}E$  and latitude  $25^{\circ}S$  to  $55^{\circ}S$ ). In Tab.1, we report the interpolation performance in terms of  
 260 RMSE (root mean square error) for the proposed EOF NN-based scheme (NNKF-EOF) and include a  
 261 comparison to the local analog data assimilation (LAF-EnKF). With a view to specifically analyzing  
 262 the relevance of NN-based parametric covariance model, we also apply an ensemble Kalman filter  
 263 with the trained dynamical model  $\mathcal{F}^{\mathcal{P}_s}$ . The reported results clearly illustrate the relevance of the  
 264 proposed NN-based scheme for the assimilation of a single patch. The proposed NN-based scheme,  
 265 which combines a NN-based formulation of the mean forecasting operator and of the associated  
 266 covariance pattern, slightly outperforms the ensemble Kalman filters, while also significantly reducing  
 267 the computational complexity induced by the generation of ensembles of size 500.

### 268 5.2. Global interpolation performance

269 We further evaluate the performance of the proposed schemes over the considered case-study  
 270 region. Tab.2 report the mean forecasting RMS error of the proposed NN-based representation  
 271 compared with local and global forecasting operator [14]. The proposed patch-level NN-based model  
 272 outperforms the benchmarked approaches by about 5-15% in terms of interpolation RMSE, which  
 273 stresses the relevance of mean dynamical model  $\mathcal{F}$ .

274 We report the mean interpolation performance in Tab. 3 and the time series of interpolation  
 275 errors illustrated in Fig. 5. The proposed NN-based scheme (PB-NNKF-EOF) leads to very significant  
 276 improvements with respect to the optimal interpolation in terms of RMSE and correlation coefficients  
 277 for both the SST and its gradient, which emphasizes fine-scale structures (e.g., relative improvement of

Assimilation method	Considered patch RMSE (°C)			
	Patch1	Patch2	Patch3	Patch4
LAF EnKF	0.50	0.25	0.22	0.39
Bi-NN-EnKF	0.55	0.23	0.22	0.30
Bi-NN-NNKF-EOF	<b>0.46</b>	<b>0.20</b>	<b>0.19</b>	<b>0.27</b>

**Table 1. Patch-level interpolation experiment:** RMSE of the reconstructed anomaly fields for the LAF EnKF (local analog forecasting based ensemble Kalman filter), Bi-NN-EnKF (Bilinear residual neural net model ( $\mathcal{F}^{\mathcal{P}_s}$ ) used in an ensemble Kalman filter), Bi-NN-NNKF (Proposed NNKF based on a bilinear residual neural net dynamical mean model).

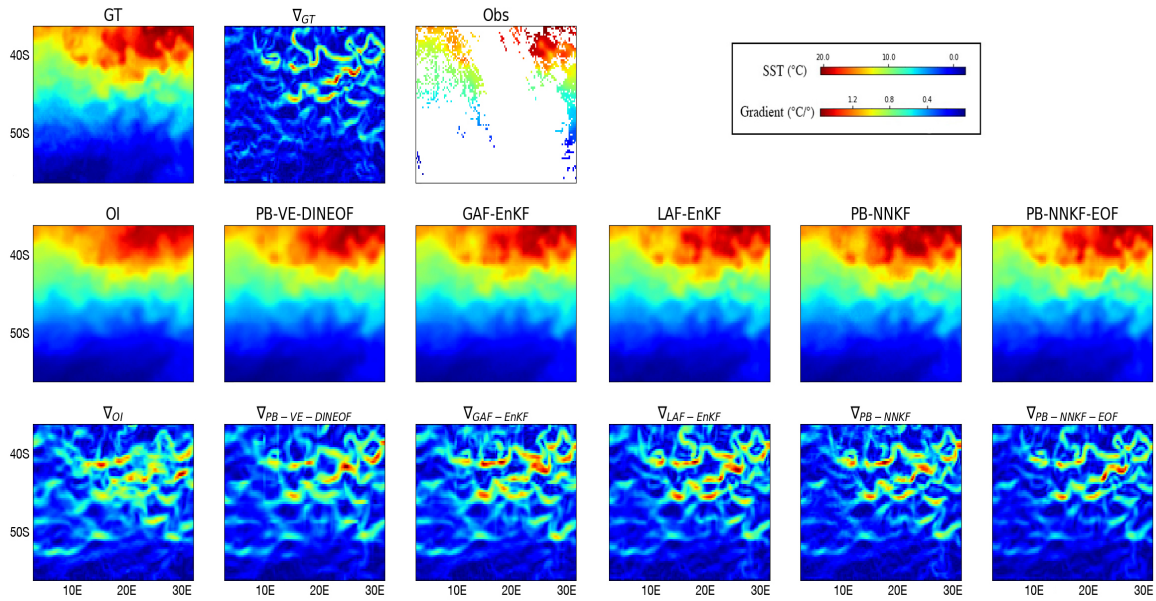


**Figure 3. Interpolation of the SST field on July 19 2015:** first row, the reference SST, its gradient and the observation with missing data (here, 82% of missing data); second row, interpolation results using respectively OI, PB-VE-DINEOF, GAN-EnKF, LAN-ENKF, PB-NN-NNKF, PB-NN-NNKF-EOF; third row, gradient of the reconstructed fields.

the RMSE above 50% for missing data areas for the SST and its gradient). A clear gain is also exhibited w.r.t. analog data assimilation and PB-VE-DINEOF schemes with a relative gain greater than 20% in terms of RMSE for both the SST and its gradient. The same conclusion holds in terms of correlation coefficients close to 90% or above for all parameters for PB-NNKF-EOF scheme, all the other ones depicting correlation coefficients below 85% for SST gradient fields. Although the considered NN-based representation exploits non-overlapping patches, we still come up with significant improvements w.r.t. AnDA schemes which involve a 50% overlapping rate between patches. This clearly illustrates the relevance of NN-based representation, which fully embeds the direct and inverse mappings between the SST field and its patch-level representation. Interestingly, Tab.3 also reveals the importance of the EOF-based parameterization of the NN-based covariance model (21) in the improvement of interpolation results w.r.t. AnDA schemes.

We further illustrate these conclusions through interpolation examples in Fig. 3. The visual analysis of the reconstructed SST gradient fields emphasize the relevance of PB-NNKF-EOF scheme to reconstruct fine-scale details. While OI and PB-VE-DINEOF schemes tend to smooth out fine-scale patterns, the analog data assimilation may not account appropriately for patch boundaries. This typically requires an empirical post-processing step [16]. By contrast, the PB-NNKF-EOF scheme fully embeds this post-processing step through reconstruction layer  $\mathcal{F}_r$  and learns its parameterization from data, which is shown here to greatly improve patch-based interpolation performance. The analysis of the spectral signatures leads to similar conclusions with the PB-NNKF-EOF scheme being the only one to recover significant energy level up to 50km.

Model	Forecasting RMSE (°C)		
	$t + h$	$t + 4h$	$t + 8h$
PB-NN	<b>0.48</b>	<b>0.60</b>	<b>0.63</b>
LAF	0.50	0.68	0.76
GAF	0.61	0.74	0.76

Table 2. Forecasting experiment for several prediction time steps

Model	Entire map				Missing data areas			
	RMSE		Correlation		RMSE		Correlation	
	SST(°C)	$\nabla$ SST(°C/°)	SST	$\nabla$ SST	SST(°C)	$\nabla$ SST(°C/°)	SST	$\nabla$ SST
PB-NNKF-EOF	<b>0.33</b>	<b>0.13</b>	<b>99.87%</b>	<b>89.30%</b>	<b>0.35</b>	<b>0.10</b>	<b>99.85%</b>	<b>93.49%</b>
PB-NNKF	0.51	0.18	99.75%	81.24%	0.51	0.18	99.71%	81.50%
LAF-EnKF	0.43	0.16	99.79%	84.41%	0.42	0.15	99.77%	86.73%
GAF-EnKF	0.48	0.19	99.74%	79.12%	0.48	0.18	99.72%	80.74%
PB-VE-DINEOF	0.54	0.20	99.68%	75.30%	0.54	0.21	99.66%	74.71%
OI	0.76	0.25	99.37%	60.31%	0.75	0.27	99.37%	55.73%

Table 3. SST interpolation experiment: Reconstruction correlation coefficient and RMSE over the SST time series and their gradient.

## 298 6. Conclusion

299 In this work, we addressed neural-network-based models for the spatio-temporal interpolation  
300 of satellite-derived SST fields with large missing data rates. We introduced a novel probabilistic

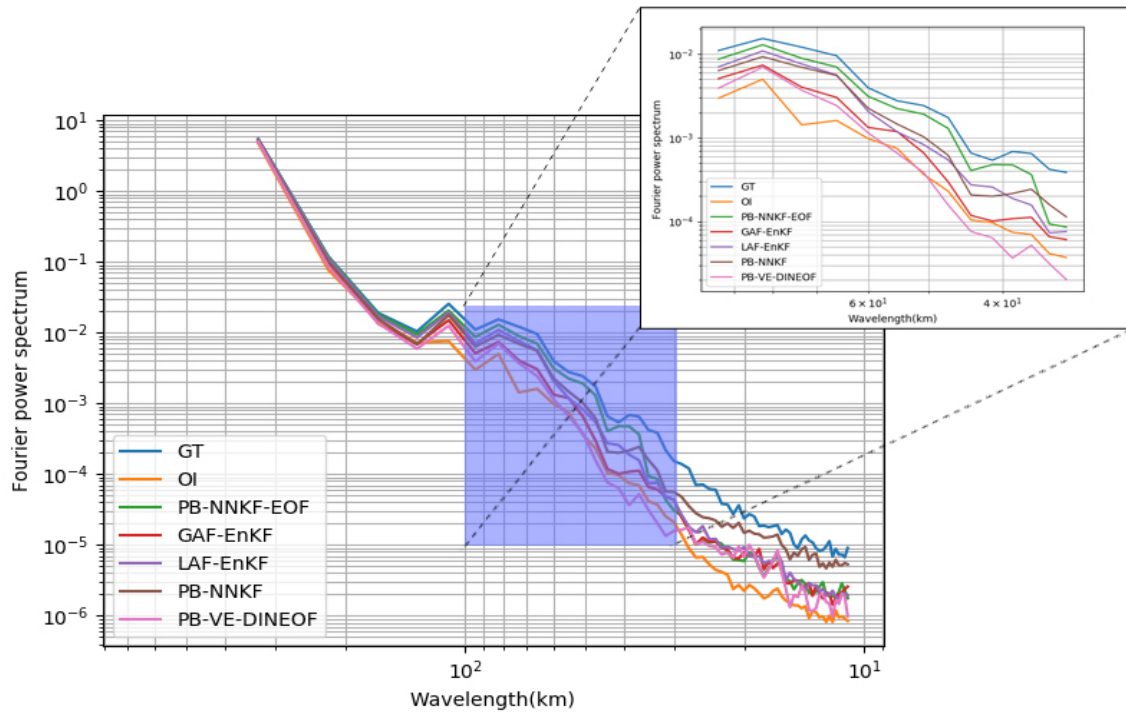


Figure 4. Radially averaged power spectral density of the interpolated SST fields with respect to the reference SST.

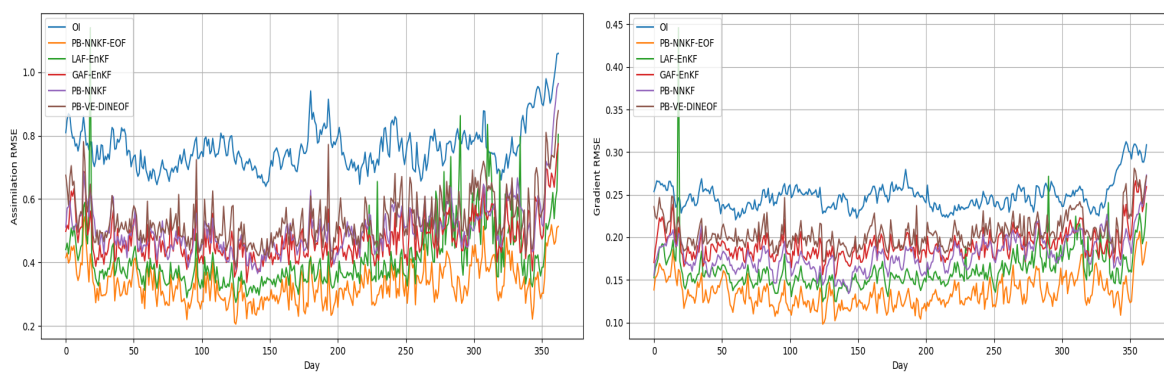


Figure 5. Interpolation RMSE times series for the selected models.

301 NN-based representation of geophysical dynamics. This representation, which relies on a patch-level  
 302 and EOF-based representation, allows us to propagate in time a mean component and the covariance  
 303 of the SST field. It makes direct the derivation of an associated Kalman filter for the spatio-temporal  
 304 interpolation of SST fields. Our numerical experiments stress a significant gain in interpolation  
 305 performance w.r.t. optimal interpolation and other state-of-the-art data-driven schemes, such DINEOF  
 306 [8] and analog data assimilation [14,16].

307 Further work could explore the application of the proposed framework to other sea surface  
 308 geophysical tracers, including multi-source and multi-modal interpolation issues. SLA (Sea Level  
 309 Anomaly) fields could provide an interesting case-study as the associated space-time sampling is  
 310 particularly scarce and multi-source strategies are of key interest [35].

311 **Author Contributions:** S.A, R.F. and C.H. stated the methodology; S.A., R.F., L.G., F.C., B.C and A.P. conceived  
 312 and designed the experiments; S.A. performed the experiments; L.G., F.C., B.C. and A.P. discussed the experiments;  
 313 R.L. and R.F. wrote the paper. B.C, A.P. and C.H. proofread the paper.

314 **Funding:** This work was supported by GERONIMO project (ANR-13-JS03-0002), Labex Cominlabs (grant SEACS),  
 315 Région Bretagne, CNES (grant OSTST-MANATEE), Microsoft (AI EU Ocean awards) and by MESR, FEDER,  
 316 Région Bretagne, Conseil Général du Finistère, Brest Métropole and Institut Mines Télécom in the framework of  
 317 the VIGISAT program managed by "Groupement Bretagne Télédétection" (BreTel).

## 318 References

- 319 1. Escudier, R.; Bouffard, J.; Pascual, A.; Poulain, P.M.; Pujol, M.I. Improvement of coastal and mesoscale  
 320 observation from space: Application to the northwestern Mediterranean Sea. *Geophysical Research Letters*  
 321 **2013**, *40*, 2148–2153. doi:10.1002/grl.50324.
- 322 2. Donlon, C.J.; Martin, M.; Stark, J.; Roberts-Jones, J.; Fiedler, E.; Wimmer, W. The Operational Sea Surface  
 323 Temperature and Sea Ice Analysis (OSTIA) system. *Remote Sensing of Environment* **2012**, *116*, 140–158.  
 324 doi:10.1016/j.rse.2010.10.017.
- 325 3. Le Traon, P.Y.; Nadal, F.; Ducet, N. An improved mapping method of multisatellite altimeter data. *Journal*  
 326 *of atmospheric and oceanic technology* **1998**, *15*, 522–534.
- 327 4. Droghei, R.; Buongiorno Nardelli, B.; Santoleri, R. A New Global Sea Surface Salinity and Density Dataset  
 328 From Multivariate Observations (1993–2016). *Frontiers in Marine Science* **2018**, *5*, 84.
- 329 5. Nardelli, B.B.; Pisano, A.; Tronconi, C.; Santoleri, R. Evaluation of different covariance models for the  
 330 operational interpolation of high resolution satellite Sea Surface Temperature data over the Mediterranean  
 331 Sea. *Remote Sensing of Environment* **2015**, *164*, 334–343.
- 332 6. Ducet, N.; Le Traon, P.Y.; Reverdin, G. Global high-resolution mapping of ocean circulation from  
 333 TOPEX/Poseidon and ERS-1 and-2. *Journal of Geophysical Research: Oceans* **2000**, *105*, 19477–19498.
- 334 7. Gomis, D.; Ruiz, S.; Pedder, M.A. Diagnostic analysis of the 3D ageostrophic circulation from a multivariate  
 335 spatial interpolation of CTD and ADCP data. *Deep Sea Research Part I: Oceanographic Research Papers* **2001**,  
 336 *48*, 269–295. doi:10.1016/S0967-0637(00)00060-1.
- 337 8. Ping, B.; Su, F.; Meng, Y. An Improved DINEOF Algorithm for Filling Missing Values in Spatio-Temporal  
 338 Sea Surface Temperature Data. *PLOS ONE* **2016**, *11*, e0155928. doi:10.1371/journal.pone.0155928.
- 339 9. Olmedo, E.; Taupier-Letage, I.; Turiel, A.; Alvera-Azcárate, A. Improving SMOS Sea Surface Salinity in the  
 340 Western Mediterranean Sea through Multivariate and Multifractal Analysis. *Remote Sensing* **2018**, *10*, 485.
- 341 10. Alvera-Azcárate, A.; Barth, A.; Parard, G.; Beckers, J.M. Analysis of SMOS sea surface salinity data using  
 342 DINEOF. *Remote sensing of environment* **2016**, *180*, 137–145.
- 343 11. Beckers, J.M.; Rixen, M. EOF Calculations and Data Filling from Incomplete  
 344 Oceanographic Datasets. *Journal of Atmospheric and Oceanic Technology* **2003**, *20*, 1839–1856.  
 345 doi:10.1175/1520-0426(2003)020<1839:ECADFF>2.0.CO;2.
- 346 12. Bertino, L.; Evensen, G.; Wackernagel, H. Sequential Data Assimilation Techniques in Oceanography.  
 347 *International Statistical Review* **2003**, *71*, 223–241. doi:10.1111/j.1751-5823.2003.tb00194.x.
- 348 13. Lorenc, A.C.; Ballard, S.P.; Bell, R.S.; Ingleby, N.B.; Andrews, P.L.F.; Barker, D.M.; Bray, J.R.; Clayton,  
 349 A.M.; Dalby, T.; Li, D.; Payne, T.J.; Saunders, F.W. The Met. Office global three-dimensional variational  
 350 data assimilation scheme. *Quarterly Journal of the Royal Meteorological Society* **2000**, *126*, 2991–3012.  
 351 doi:10.1002/qj.49712657002.

- 352 14. Lguensat, R.; Tandeo, P.; Ailliot, P.; Pulido, M.; Fablet, R. The Analog Data Assimilation. *Monthly Weather*  
353 *Review* **2017**. doi:10.1175/MWR-D-16-0441.1.
- 354 15. Lguensat, R.; Huynh Viet, P.; Sun, M.; Chen, G.; Fenglin, T.; Chapron, B.; FABLET, R. Data-driven  
355 Interpolation of Sea Level Anomalies using Analog Data Assimilation.
- 356 16. Fablet, R.; Viet, P.H.; Lguensat, R. Data-Driven Models for the Spatio-Temporal Interpolation  
357 of Satellite-Derived SST Fields. *IEEE Transactions on Computational Imaging* **2017**, *3*, 647–657.  
358 doi:10.1109/TCI.2017.2749184.
- 359 17. Tandeo, P.; Ailliot, P.; Chapron, B.; Lguensat, R.; Fablet, R. The analog data assimilation: application  
360 to 20 years of altimetric data. *International Workshop on Climate Informatics*; , 2015; pp. 1 – 2.  
361 doi:10.13140/RG.2.1.4030.5681.
- 362 18. Egmont-Petersen, M.; de Ridder, D.; Handels, H. Image processing with neural networks—a review.  
363 *Pattern Recognition* **2002**, *35*, 2279–2301. doi:10.1016/S0031-3203(01)00178-9.
- 364 19. Fablet, R.; Ouala, S.; Herzet, C. Bilinear residual Neural Network for the identification and forecasting of  
365 dynamical systems. *SciRate* **2017**.
- 366 20. Braakmann-Folgmann, A.; Roscher, R.; Wenzel, S.; Uebbing, B.; Kusche, J. Sea Level Anomaly Prediction  
367 using Recurrent Neural Networks. *arXiv:1710.07099 [cs]* **2017**. arXiv: 1710.07099.
- 368 21. He, K.; Zhang, X.; Ren, S.; Sun, J. Deep Residual Learning for Image Recognition. *arXiv:1512.03385 [cs]*  
369 **2015**. arXiv: 1512.03385.
- 370 22. Mairal, J.; Sapiro, G.; Elad, M. Learning multiscale sparse representations for image and video restoration.  
371 *Multiscale Modeling & Simulation* **2008**, *7*, 214–241.
- 372 23. Evensen, G. *Data Assimilation*; Springer Berlin Heidelberg: Berlin, Heidelberg, 2009.  
373 doi:10.1007/978-3-642-03711-5.
- 374 24. Bertino, L.; Evensen, G.; Wackernagel, H. Sequential Data Assimilation Techniques in Oceanography.  
375 *International Statistical Review* **2007**, *71*, 223–241. doi:10.1111/j.1751-5823.2003.tb00194.x.
- 376 25. Anderson, J.L.; Anderson, S.L. A Monte Carlo Implementation of the Nonlinear Filtering Problem  
377 to Produce Ensemble Assimilations and Forecasts. *Monthly Weather Review* **1999**, *127*, 2741–2758.  
378 doi:10.1175/1520-0493(1999)127<2741:AMCIOT>2.0.CO;2.
- 379 26. Houtekamer, P.L.; Mitchell, H.L. Data Assimilation Using an Ensemble Kalman Filter Technique. *Monthly*  
380 *Weather Review* **1998**, *126*, 796–811. doi:10.1175/1520-0493(1998)126<0796:DAUAEK>2.0.CO;2.
- 381 27. Gaspari, G.; Cohn, S.E. Construction of correlation functions in two and three dimensions. *Quarterly*  
382 *Journal of the Royal Meteorological Society* **1999**, *125*, 723–757. doi:10.1002/qj.49712555417.
- 383 28. Houtekamer, P.L.; Mitchell, H.L. A Sequential Ensemble Kalman Filter for Atmospheric Data Assimilation.  
384 *Monthly Weather Review* **2001**, *129*, 123–137. doi:10.1175/1520-0493(2001)129<0123:ASEKFF>2.0.CO;2.
- 385 29. Bocquet, M. Localization and the iterative ensemble Kalman smoother. *Quarterly Journal of the Royal*  
386 *Meteorological Society* **2016**, *142*, 1075–1089. doi:10.1002/qj.2711.
- 387 30. Pannekoucke, O.; Emili, E.; Thual, O. Modelling of local length-scale dynamics and isotropizing  
388 deformations. *Quarterly Journal of the Royal Meteorological Society* **2013**, *140*, 1387–1398. doi:10.1002/qj.2204.
- 389 31. Pannekoucke, O.; Ricci, S.; Barthelemy, S.; Ménard, R.; Thual, O. Parametric Kalman filter  
390 for chemical transport models. *Tellus A: Dynamic Meteorology and Oceanography* **2016**, *68*, 31547.  
391 doi:10.3402/tellusa.v68.31547.
- 392 32. Cohn, S.E. Dynamics of Short-Term Univariate Forecast Error Covariances. *Monthly Weather Review* **1993**,  
393 *121*, 3123–3149. doi:10.1175/1520-0493(1993)121<3123:DOSTUF>2.0.CO;2.
- 394 33. LeCun, Y.; Haffner, P.; Bottou, L.; Bengio, Y. Object Recognition with Gradient-Based Learning. In  
395 *Shape, Contour and Grouping in Computer Vision*; Forsyth, D.A.; Mundy, J.L.; di Gesù, V.; Cipolla, R., Eds.;  
396 *Lecture Notes in Computer Science*, Springer Berlin Heidelberg: Berlin, Heidelberg, 1999; pp. 319–345.  
397 doi:10.1007/3-540-46805-6\_19.
- 398 34. Ouala, S.; Herzet, C.; Fablet, R. Sea surface temperature prediction and reconstruction using patch-level  
399 neural network representations. *arXiv:1806.00144 [cs, stat]* **2018**. arXiv: 1806.00144.
- 400 35. Fablet, R.; Verron, J.; Mourre, B.; Chapron, B.; Pascual, A. Improving Mesoscale Altimetric Data From  
401 a Multitracer Convolutional Processing of Standard Satellite-Derived Products. *IEEE Transactions on*  
402 *Geoscience and Remote Sensing* **2018**, *56*, 2518–2525. doi:10.1109/TGRS.2017.2750491.

403 © 2018 by the authors. Submitted to *Remote Sens.* for possible open access publication  
404 under the terms and conditions of the Creative Commons Attribution (CC BY) license  
405 (<http://creativecommons.org/licenses/by/4.0/>).